



This is the accepted manuscript made available via CHORUS. The article has been published as:

Effect of structural disorder on the Kitaev magnet $\mathcal{M}_{AgMn_3Li_2O_6}$

Faranak Bahrami, Eric M. Kenney, Chennan Wang, Adam Berlie, Oleg I. Lebedev, Michael J. Graf, and Fazel Tafti

Phys. Rev. B **103**, 094427 — Published 17 March 2021

DOI: [10.1103/PhysRevB.103.094427](https://doi.org/10.1103/PhysRevB.103.094427)

Effect of structural disorder on the Kitaev magnet $\text{Ag}_3\text{LiIr}_2\text{O}_6$

Faranak Bahrami,¹ Eric M. Kenney,¹ Chennan Wang,²

Adam Berlie,³ Oleg I. Lebedev,⁴ Michael J. Graf,¹ and Fazel Tafti¹

¹*Department of Physics, Boston College, Chestnut Hill, MA 02467, USA*

²*Laboratory for Muon Spin Spectroscopy, Paul Scherrer Institute, CH-5232 Villigen, Switzerland*

³*ISIS Neutron and Muon Source, Science and Technology Facilities Council, Rutherford Appleton Laboratory, Didcot, OX11 0QX, United Kingdom*

⁴*Laboratoire CRISMAT, ENSICAEN-CNRS UMR6508, 14050 Caen, France*

(Dated: March 2, 2021)

The search for an ideal Kitaev spin liquid candidate with anyonic excitations and long-range entanglement has motivated the synthesis of a new family of intercalated Kitaev magnets such as $\text{H}_3\text{LiIr}_2\text{O}_6$, Cu_2IrO_3 , and $\text{Ag}_3\text{LiIr}_2\text{O}_6$. The absence of a susceptibility peak and a two-step release of the magnetic entropy in these materials have been proposed as evidence of proximity to the Kitaev spin liquid. Here we present a comparative study of the magnetic susceptibility, heat capacity, and muon spin relaxation (μSR) between two samples of $\text{Ag}_3\text{LiIr}_2\text{O}_6$ in the clean and disordered limits. In the disordered limit, the absence of a peak in either susceptibility or heat capacity and the lack of zero field muon precession in the μSR signal give the impression of a proximate spin liquid state. However, in the clean limit, peaks are resolved in both susceptibility and heat capacity, and spontaneous oscillations appear in the μSR signal, confirming long-range antiferromagnetic order in the ground state. The μSR oscillations fit to a Bessel function, characteristic of incommensurate order, as reported in the parent compound $\alpha\text{-Li}_2\text{IrO}_3$. Our results clarify the role of structural disorder in the intercalated Kitaev magnets.

I. INTRODUCTION

A long standing challenge in condensed matter physics has been to access a quantum spin liquid (QSL) ground state characterized by long-range entanglement and fractionalized anyonic excitations¹⁻³. One of the most promising theoretical models of QSL is the Kitaev model based on interacting spin-1/2 ions on a 2D honeycomb lattice with bond-dependent Ising axes⁴. The prime candidates for the Kitaev model are $\alpha\text{-Li}_2\text{IrO}_3$, Na_2IrO_3 , and $\alpha\text{-RuCl}_3$, but all three compounds order magnetically at low temperatures⁵⁻¹⁰. Recently, a new class of intercalated Kitaev magnets have been synthesized via a topochemical exchange of the interlayer Li/Na atoms in $\alpha\text{-Li}_2\text{IrO}_3$ and Na_2IrO_3 with H, Cu, or Ag atoms, and producing $\text{H}_3\text{LiIr}_2\text{O}_6$, $\text{Cu}_3\text{LiIr}_2\text{O}_6$, Cu_2IrO_3 , and $\text{Ag}_3\text{LiIr}_2\text{O}_6$ ¹¹⁻¹⁵. It is claimed that this new family of Kitaev magnets, specifically $\text{H}_3\text{LiIr}_2\text{O}_6$ and $\text{Ag}_3\text{LiIr}_2\text{O}_6$, are closer to the QSL phase based on the absence of magnetic ordering in thermodynamic measurements, a scaling behavior in the heat capacity, and a two-step release of the magnetic entropy^{11,14,16,17}. Both bond disorder and modified interlayer coordination are hypothesized as possible mechanisms for the proximity to the QSL ground state^{13,14,17,18}. Currently, there is no careful experimental work to examine these hypotheses and elucidate the role of structural disorder in the intercalated Kitaev magnets.

In this article, we present a careful study on the effect of structural disorder on one of the intercalated Kitaev magnets, $\text{Ag}_3\text{LiIr}_2\text{O}_6$. We show that the signatures of magnetic ordering may be hidden in a disordered sample, but they emerge unmistakably in a clean sample. Based on our experimental results, the onset of magnetic

ordering in the clean limit is unaffected by the interlayer coordination, and the nature of disorder in $\text{Ag}_3\text{LiIr}_2\text{O}_6$ is inconsistent with a randomized bond picture¹⁷. Our experimental discussion is organized in four sections. First, in a clean sample (S1), we reveal a peak in the magnetic susceptibility at the Néel temperature $T_N = 14$ K followed by a sharper downturn at $T_{\text{LRO}} = 8$ K. Such a peak is absent in a disordered sample (S2). Second, we also reveal a peak in the heat capacity of S1 at T_N , which turns into a mild change of slope in S2. In the light of these findings, we will revisit the two-step entropy release that has been interpreted as evidence of spin fractionalization in $\text{Ag}_3\text{LiIr}_2\text{O}_6$, $\alpha\text{-Li}_2\text{IrO}_3$, Na_2IrO_3 , and $\alpha\text{-RuCl}_3$ ^{14,19,20}. Third, using muon spin relaxation (μSR) measurements, we show that T_N marks the onset of an incommensurate magnetic order with short-range correlations that become long-range below T_{LRO} in the clean sample S1. The μSR oscillations are not visible in sample S2. Fourth, we use transmission electron microscopy (TEM) to reveal extended regions of silver inclusion within the honeycomb layers of S2 that are absent in S1. Complementary data and analyses are presented in four appendices at the end.

II. EXPERIMENTAL METHODS

$\text{Ag}_3\text{LiIr}_2\text{O}_6$ was synthesized via a topotactic cation-exchange reaction as reported in Ref.¹⁴. To improve the sample quality, however, we took two important additional measures. First, we minimized the stacking faults in the precursor $\alpha\text{-Li}_2\text{IrO}_3$ by performing a sequential solid-state synthesis at 900, 1000, and 1015 °C for 24, 32, and 48 h, respectively. Second, we increased the duration of the topotactic reaction to several days to ensure

a complete exchange of the high-quality α - Li_2IrO_3 precursor (see also Appendix A). Sample S1 was made with the improved technique and sample S2 was made with the methods described in Ref.¹⁴.

The electron diffraction (ED) and high angle annular dark field scanning TEM (HAADF-STEM) were performed using an aberration corrected JEM ARM200F microscope. Powder X-ray diffraction (PXR) was performed using a Bruker D8 ECO instrument equipped with a Cu- K_α source and a 1D LINXEYE-XE detector. Magnetization and heat capacity were measured using Quantum Design MPMS3 and Dynacool PPMS, respectively.

The μSR experiments were carried at the Paul Scherrer Institute (PSI) using a ^3He refrigerator with the Dolly Multi Purpose Surface-Muon Instrument (sample S1), and a gas flow cryostat with the General Purpose Surface-Muon (GPS) Instrument (both samples). The Musfit program²¹ was used for data analysis. Sample S1 was pressed into a pellet 13 mm in diameter and 1 mm thick, and sample S2 was 13 mm in diameter and 1.2 mm thick. The pellets were wrapped in a 25 μm thin silver foil and mounted with varnish on copper holders. The same holder was used to mount S1 in both spectrometers. Initial measurements were made on sample S2 using a dilution refrigerator and gas flow cryostat on the EMU spectrometer at the ISIS Muon Source at the Rutherford Appleton Laboratory.

III. RESULTS AND DISCUSSION

A. Magnetic Susceptibility

The first evidence of magnetic ordering in a high-quality $\text{Ag}_3\text{LiIr}_2\text{O}_6$ sample (S1) is a peak at $T_N=14$ K in the DC susceptibility (χ) as seen in Fig. 1(a) and magnified in Fig. 1(b). **A similar behavior has been observed in an earlier work by Todorova *et al.*¹⁵** The peak is broad and shows splitting between the zero-field-cooled (ZFC) and field-cooled (FC) conditions (inset of Fig. 1a and Appendix B). A second temperature scale in Fig. 1(b) is $T_{\text{LRO}}=8$ K, below which, the susceptibility visibly turns down (and the μSR data reveal clear oscillations in Section III C). Thus, we identify T_N as the onset of short-range magnetic ordering that becomes long-range below T_{LRO} .

We compare the magnetic susceptibility of the clean sample (S1) and disordered sample (S2) in Fig. 1(c). A susceptibility peak is present in the former, but absent in the latter. The absence of such a peak in a sample with the same quality as S2 has been misinterpreted as evidence of proximity to a Kitaev spin liquid¹⁴. After tremendous efforts to remove disorder and improve the quality of $\text{Ag}_3\text{LiIr}_2\text{O}_6$, we were able to resolve the AFM peak in the high-quality sample S1. Based on our results, it would be insightful to revisit recent claims of a quantum spin liquid phase in another Kitaev material

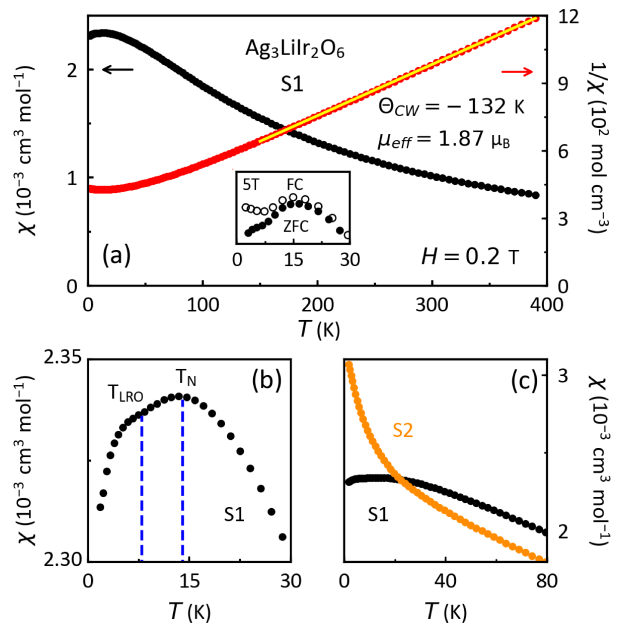


FIG. 1. (a) DC magnetic susceptibility per mole Ir (black data) and inverse susceptibility (red data) plotted as a function of temperature in the high-quality sample S1. The yellow line is a Curie-Weiss fit at $T > 150$ K. The full and open circles in the inset represent the zero-field-cooled (ZFC) and field-cooled (FC) curves at $H = 5$ T. (b) Magnified view of the ZFC susceptibility from sample S1 showing a broad peak at $T_N = 14$ K and a sharper downturn at $T_{\text{LRO}} = 8$ K. (c) $\chi(T)$ curves are compared between the clean sample S1 (black points) and disordered sample S2 (orange data from Ref.¹⁴).

$\text{H}_3\text{LiIr}_2\text{O}_6$ which suffers from a higher disorder level than $\text{Ag}_3\text{LiIr}_2\text{O}_6$ ^{11,22}. A large low-temperature tail in $\chi(T)$ has been observed in $\text{H}_3\text{LiIr}_2\text{O}_6$ similar to the behavior of sample S2 in Fig. 1(c). The question is whether a peak is hidden under that low-temperature tail. In a similar vein, recent claims of a disordered QSL phase in Cu_2IrO_3 based on the absence of a peak in $\chi(T)$ may be questionable¹⁸. In fact, a small peak at 2 K has been reported in higher-quality samples of that material and diagnosed as a signature of partial static magnetism²³.

To understand the magnetic interactions in $\text{Ag}_3\text{LiIr}_2\text{O}_6$, we performed a Curie-Weiss (CW) analysis on the inverse susceptibility ($1/\chi$) in Fig. 1(a). The yellow line represents the CW fit that yields a CW temperature $\Theta_{\text{CW}}=-132(1)$ K and a magnetic moment $\mu_{\text{eff}}=1.87(2)$ μ_B . The negative sign of Θ_{CW} indicates AFM interactions and its large magnitude, compared to T_N , implies magnetic frustration²⁴. We extract an effective magnetic moment of $\mu_{\text{eff}}=1.87$ μ_B from the CW fit which is comparable to the reported values in other Kitaev magnets^{13,19} and close to the expected moment for a $J_{\text{eff}}=1/2$ state (1.74 μ_B). The values of μ_{eff} and Θ_{CW} are comparable between S1 (1.87 μ_B , -132 K) and S2 (1.79 μ_B , -142 K)¹⁴.

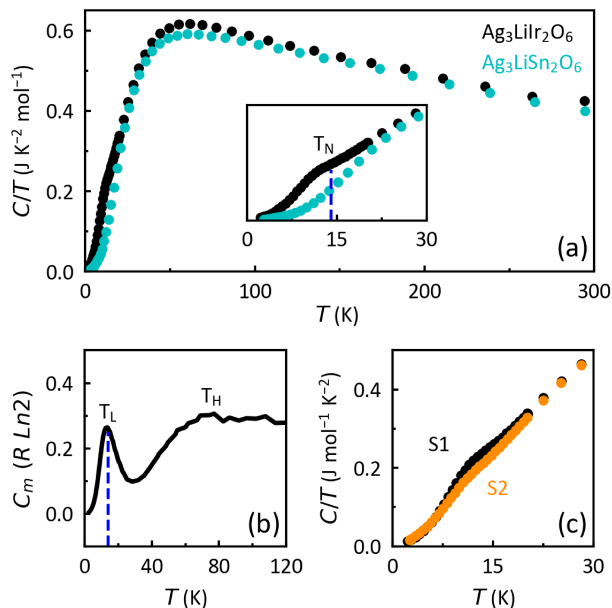


FIG. 2. (a) Heat capacity divided by temperature (C/T) per mole Ir or Sn plotted as a function of temperature in $\text{Ag}_3\text{LiIr}_2\text{O}_6$ (black data) and its nonmagnetic lattice model $\text{Ag}_3\text{LiSn}_2\text{O}_6$ (turquoise data from ref.¹⁴). (b) Magnetic heat capacity (C_m) in units of $R \ln(2)$ as a function of temperature below 120 K in S1, where $T_L = T_N = 14$ K and $T_H = 75$ K. (c) Comparison between C/T as a function of temperature below 30 K in the clean sample S1 (black) and disordered sample S2 (orange). The orange curve (from Ref.¹⁴) is shifted by -0.014 K for clarity.

B. Heat Capacity

We measured the heat capacity (C) of sample S1 to confirm the bulk AFM order in $\text{Ag}_3\text{LiIr}_2\text{O}_6$. Figure 2(a) shows a broad peak in C/T at $T_N = 14$ K, consistent with the peak at 14 K in $\chi(T)$. On the same figure, we also present the heat capacity of an isostructural compound $\text{Ag}_3\text{LiSn}_2\text{O}_6$ which serves as a non-magnetic lattice model for $\text{Ag}_3\text{LiIr}_2\text{O}_6$. The two data sets closely track each other as a function of temperature, except near 75 K and 14 K, where an additional magnetic contribution enhances the heat capacity of $\text{Ag}_3\text{LiIr}_2\text{O}_6$. The magnetic heat capacity (C_m) can be isolated by subtracting the $\text{Ag}_3\text{LiSn}_2\text{O}_6$ data from $\text{Ag}_3\text{LiIr}_2\text{O}_6$. Figure 2(b) shows C_m in units of $R \ln(2)$ as a function of temperature where two broad peaks are resolved at a higher $T_H = 75$ K and a lower $T_L = 14$ K temperature. Such a behavior has been interpreted as evidence of a fractionalization of spins into Majorana fermions at T_H followed by a long-range entanglement at T_L in $\text{Ag}_3\text{LiIr}_2\text{O}_6$, $\alpha\text{-Li}_2\text{IrO}_3$, Na_2IrO_3 , and $\alpha\text{-RuCl}_3$ ^{14,19,20}, based on a quantum Monte Carlo simulation of the Kitaev Hamiltonian²⁵. We caution against this interpretation and point out that the peak at $T_L = T_N$ in $\text{Ag}_3\text{LiIr}_2\text{O}_6$ is due to static magnetism instead of quantum entanglement.

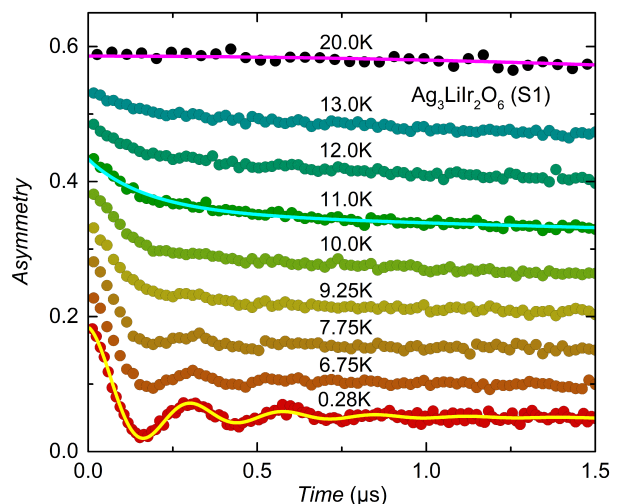


FIG. 3. Asymmetry plotted as a function of time at short timescales. The curves have been offset by equal increments from the base-temperature curve (0.28 K) for clarity. The magenta, cyan, and yellow solid lines are fits to Eq. 1, Eq. 2, and Eq. 3, respectively.

We compare the C/T curves between samples S1 (clean) and S2 (disordered) in Fig. 2(c). Whereas S2 shows a slight change of slope at $T_N = 14$ K, S1 reveals a peak. Notice that without having the clean sample S1, the heat capacity of S2 could have been misinterpreted as the absence of magnetic ordering. This shows the importance of improving sample quality, since without having access to S1, we could not have associated the peak at T_L with the entropy release from a long-range AFM order instead of entanglement. Similarly, the low temperature peaks in the heat capacity of $\alpha\text{-Li}_2\text{IrO}_3$, Na_2IrO_3 , and $\alpha\text{-RuCl}_3$ are due to AFM ordering^{14,19,20}.

The above discussion does not discredit the iridate materials as candidates of a Kitaev spin liquid. Note that the peak at T_H may indeed signal the onset of a fractionalization process, but the Majorana liquid develops an instability toward a gapped AFM state instead of melting into an entangled spin liquid ground state. In $\alpha\text{-RuCl}_3$, this instability is removed by applying a 7 T magnetic field parallel to the honeycomb planes²⁶. A similar effect may be observed in $\text{Ag}_3\text{LiIr}_2\text{O}_6$ once single crystals are available.

C. Muon Spin Relaxation (μSR)

In positive muon spin relaxation ($\mu^+\text{SR}$), spin-polarized positive muons are injected into a sample and in less than 1 ps come to rest at a preferred crystallographic interstitial site (or sites). The muon spin polarization then evolves with time in the local magnetic field, yielding information about the magnitude and orientation of the local field relative to the initial spin direction. After tens of millions of decay events, a time histogram can be

used to extract the asymmetry, which is proportional to the time dependence of the projection of the muon spin along the detector direction²⁷. The asymmetry contains information about the local fields temporal and spatial variation.

We plot the asymmetry as a function of time in sample S1 in Fig. 3, at nine representative temperatures from 0.28 to 20 K at zero field. For temperatures greater than or equal to 20 K, the Ir⁴⁺ moments are fluctuating too rapidly, and they have no effect on the muon. Therefore, the depolarization is dominated by randomly oriented quasistatic nuclear moments. The temperature dependent asymmetry is well described by a Gaussian Kubo-Toyabe function

$$A_{\text{KT}}(t) = A_0 \left[\frac{1}{3} + \frac{2}{3} (1 - \sigma^2 t^2) \exp\left(-\frac{1}{2} \sigma^2 t^2\right) \right] \quad (1)$$

where $A_0 = 0.174$ is the initial asymmetry for GPS in spin-rotated mode, and the parameter $\sigma = 0.150$ MHz is proportional to the second moment of the field distribution experienced by the muon ensemble. The magenta line on Fig. 3 is a fit to Eq. 1 at 20 K. We found a constant value for σ between 200 and 20 K, indicating that the muon is not diffusing in this temperature range. The data below 20 K can be explained in three regions of interest.

Region 1. For $20 \text{ K} > T > T_N$, depolarization is dominated by the nuclear moments. The electronic moments are slowing down and begin contributing to muon depolarization.

Region 2. For the range $T_N > T > T_{\text{LRO}}$, depolarization is dominated by the electronic moments. Short-range correlations are manifested in the onset of a fast relaxation component in addition to a slow exponential depolarization due to fluctuations. To characterize the crossover in this temperature range, we use a phenomenological depolarization function

$$A(t) = A_0 \left[\alpha_F \exp\left(-(\lambda_F t)^\beta\right) + (1 - \alpha_F) \exp(-\lambda_S t) \right] \quad (2)$$

where $A_0 = 0.185$ is the initial asymmetry in the Dolly spectrometer in spin-rotated mode. The first term in the brackets is related to the fast decay with rate λ_F best described by a stretched exponential with exponent β , and attributed to spin freezing. The second term is a slow exponential decay at rate λ_S attributed to a fluctuating contribution. The fit parameters λ_F , β , and λ_S in sample S1 vary from $10.1(6) \mu\text{s}^{-1}$, $0.85(6)$, and $0.211(2) \mu\text{s}^{-1}$ at 13 K, respectively, to $11.0(1) \mu\text{s}^{-1}$, $1.75(5)$, and $0.285(8) \mu\text{s}^{-1}$ at 8 K.

The cyan line on Fig. 3 is a representative fit to Eq. 2 at 11 K. From such fits, we extract the fraction of fast decay α_F , which we take as a metric for the onset of static magnetism. The temperature dependence of α_F is plotted in Fig. 4(a), and it vanishes near $T_N = 14$ K.

We compare the polarization (normalized asymmetry) at 10 K between samples S1 and S2 in Fig. 4(b). At this

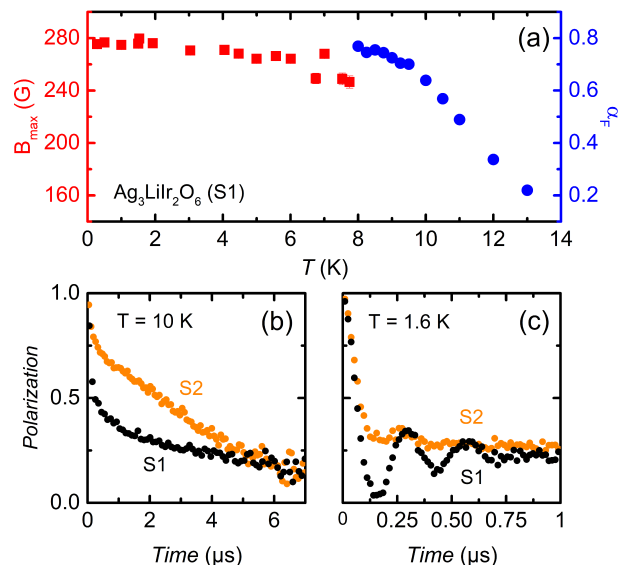


FIG. 4. (a) The blue circles represent α_F values from fits to Eq. 2, and the red squares represent B_{max} values from fits to Eq. 3 in the clean sample S1. Static magnetism starts at $T_N = 14$ K and μSR oscillations start at $T_{\text{LRO}} = 8$ K. (b) Muon polarization ($P = A/A_0$ where A_0 is the initial asymmetry) as a function of time in S1 and S2 at 10 K ($T_N > T > T_{\text{LRO}}$). (c) Polarization curves below $1 \mu\text{s}$ in S1 and S2 at 1.6 K ($T < T_{\text{LRO}}$). The oscillations are barely discernible in the disordered sample S2, although the initial depolarization is comparable between S1 and S2.

temperature ($T_N > T > T_{\text{LRO}}$), neither S1 nor S2 shows oscillations; however, the fast decay below $1 \mu\text{s}$ is visibly faster in S1. Note that the long-time tail of polarization converges to the same value in both samples, indicating weak dynamics. We conclude that the same magnetic ordering starts below T_N in both samples, but the short-range correlations are stronger in S1 evidenced by larger λ_F than in S2.

Region 3. At $T < T_{\text{LRO}}$, clear oscillations appear in the depolarization curves of S1 (Fig. 3), indicating a long-range magnetic order. The depolarization curves are well described by the function

$$A_{\text{LRO}}(t) = A_0 [\alpha_{\text{LRO}} \exp(-\Lambda t) J_0(\gamma_\mu B_{\text{max}} t + \phi) + (1 - \alpha_{\text{LRO}}) \exp(-\lambda t)] \quad (3)$$

Again, the initial asymmetry is $A_0 = 0.185$ in the Dolly spectrometer. Here J_0 is the zeroth-order Bessel function and the muon gyromagnetic ratio is $\gamma_\mu = 2\pi(135.5 \text{ MHz/T})$. The yellow line on Fig. 3 is a fit to the Bessel function at 0.28 K. A Bessel oscillatory behavior is typically associated with incommensurate magnetic ordering²⁷, where the muon experiences ordered fields ranging from 0 to B_{max} . We extract the B_{max} value from such a fit at each temperature below T_{LRO} , and plot it in Fig. 4(a) as red squares. Such an analysis would be impossible for the disordered sample S2 as can be seen from the comparison in Fig. 4(c). The oscillations are barely

visible in S2, thus a fit to Eq. 3 would not work. Two additional observations in Fig. 4(c) are worth noting. First, at extremely short timescale (less than $0.1 \mu\text{s}$), the fast depolarization is identical in both samples. Second, the long-time depolarization tail ($t > 0.8 \mu\text{s}$) converges between the two samples. From these observations, we conclude that a similar incommensurate order exists in the ground state of both samples, but with a longer correlation length in sample S1 than in S2, due to less disorder.

At the base temperature $T = 0.28 \text{ K}$, the fit to Eq. 3 yields $\alpha_{\text{LRO}} = 0.741(2)$, $B_{\text{max}} = 269(1) \text{ G}$, $\phi = -0.9(6)^\circ$, $\Lambda = 2.8(1) \mu\text{s}^{-1}$, and $\lambda = 0.052(4) \mu\text{s}^{-1}$. The value for α_{LRO} is close to the value $2/3$ expected from a polycrystalline sample exhibiting long-range magnetic order. The value for B_{max} is confirmed from a longitudinal field (LF) experiment in Appendix C. The damping rate λ is associated with those muons whose initial polarization lies along the local magnetic field and are depolarized by transverse magnetic fluctuations. The rate Λ contains contributions from both static magnetic disorder and magnetic fluctuations. Since $\Lambda \gg \lambda$, disorder is the dominant contribution.

D. Transmission Electron Microscopy (TEM)

So far, we have presented the magnetic behavior of $\text{Ag}_3\text{LiIr}_2\text{O}_6$ in the clean (S1) and disordered (S2) limits using both bulk and local probes. Here we characterize the structural disorder in the material using high-resolution HAADF-STEM images from both samples S1 and S2 in Fig. 5. The characteristic feature of each honeycomb layer in Fig. 5(a,b) is a repeating pattern of a pair of Ir atoms (large bright spots) separated by a Li atom (not visible). This pattern is interrupted in sample S2 by rows of unwanted Ag atoms (smaller bright spots) as indicated by the arrows in Fig. 5(a). Note that silver inclusions take the form of extended defects (rows of Ag atoms) instead of local defects (singular intersite disorder). The distinction between local and extended defects are important especially in theoretical modeling of disordered Kitaev magnets²⁸.

In the inset of Fig. 5(a), a crystallographic model is overlaid on the magnified image to identify the Ag, Ir, Li, and O atoms as blue, yellow, pink, and red spheres, respectively (only the Ag and Ir atoms are clearly visible). The arrows indicate where the unwanted Ag atoms (blue) are inserted within the Ir layer (yellow). In contrast, the HAADF-STEM image from the clean sample S1 in Fig. 5(b) shows pristine honeycomb layers free from silver inclusions.

We present the electron diffraction (ED) patterns for S1 and S2 in the top insets of Fig. 5(a,b). The streaking in ED patterns is due to the stacking faults in the form of angular twist between the adjacent layers as shown in other honeycomb materials²⁹. Upon careful inspection, the ED pattern of sample S1 reveals less streaking than S2. This is consistent with the synthesis of sam-

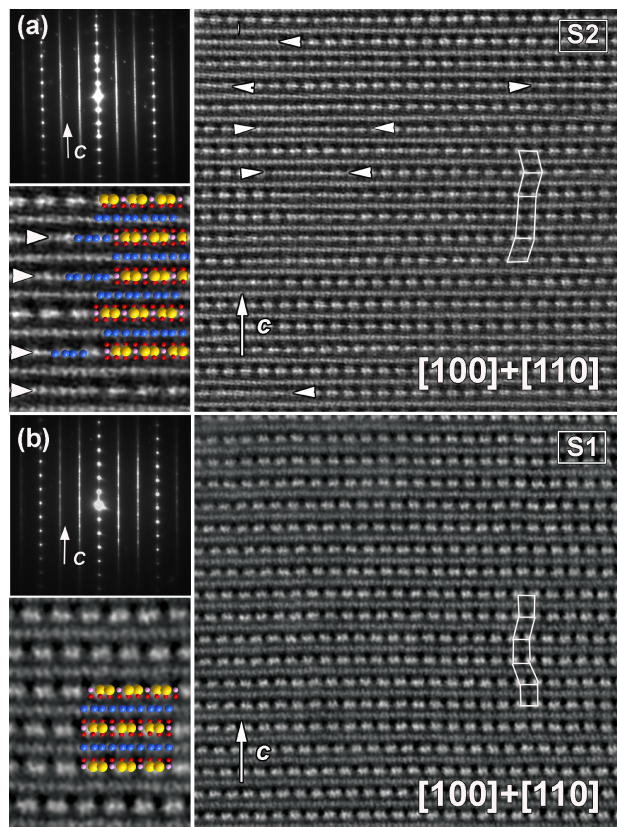


FIG. 5. (a) Electron diffraction (top inset) and HAADF-STEM image from the disordered sample S2. A structural model is overlaid on the magnified image in the bottom inset with blue, yellow, pink, and red spheres for the Ag, Ir, Li, and O atoms, respectively. The arrows indicate where Ag atoms replace Ir atoms within the honeycomb layers. (b) Similar images from the clean sample S1 where Ag inclusion is absent.

ple S1 from a precursor $\alpha\text{-Li}_2\text{IrO}_3$ with fewer stacking faults as explained in Appendix A (Fig. 6). We show in Appendix D (Fig. 9) that $\text{Ag}_3\text{LiIr}_2\text{O}_6$ has more stacking faults than its parent compounds $\alpha\text{-Li}_2\text{IrO}_3$. It is likely that in the absence of such stacking faults, the initial spin freezing at T_N could turn into a long-range order, i.e. $T_N = T_{\text{LRO}}$ ³⁰.

IV. CONCLUSION

By improving the sample quality, we have revealed signatures of a long-range incommensurate order in $\text{Ag}_3\text{LiIr}_2\text{O}_6$. A broad peak in the magnetic susceptibility and heat capacity at $T_N=14 \text{ K}$ marks the onset of magnetic ordering. Such a peak is absent in the disordered sample, which hinders the recognition of a long-range order in $\text{Ag}_3\text{LiIr}_2\text{O}_6$. In μSR , a fast decay of muon depolarization below T_N shows the onset of short-range order, and the appearance of oscillations below T_{LRO} confirms the long-range order. The oscillation patterns at low tem-

peratures fit to a Bessel function, consistent with incommensurate ordering. An incommensurate spiral order has been confirmed in α - Li_2IrO_3 from both μSR and neutron scattering³¹. Our HAADF-STEM images confirm a moderate level of extended defects (silver inclusion) in the disordered $\text{Ag}_3\text{LiIr}_2\text{O}_6$ sample made from a lower quality α - Li_2IrO_3 . In the disordered sample, the Ag atoms enter the honeycomb layer and disrupt the long-range magnetic order. This effect must be distinguished from the lack of magnetic ordering due to long-range entanglement in a quantum spin liquid.

ACKNOWLEDGMENTS

The first two authors have contributed equally to this work. We thank R. Valenti and N. B. Perkins for fruitful discussions, and H. Luetkens, T. Shiroka and C. Baines for their technical assistance with the μSR experiments. The work at Boston College was supported by the National Science Foundation under award No. DMR-1708929. This work is based on experiments performed at the Swiss Muon Source $S\mu\text{S}$ at the Paul Scherrer Institute, Villigen, Switzerland, and at the ISIS Pulsed Muon Source, which is supported by the UK Science and Technology Facilities Council.

Appendix A: Synthesis details.

The important difference between the two $\text{Ag}_3\text{LiIr}_2\text{O}_6$ samples, S1 and S2, is in the α - Li_2IrO_3 precursor used in their synthesis. Figure 6(a) compares the x-ray patterns between two α - Li_2IrO_3 precursors, shown in black and red, used for the synthesis of samples S1 (clean) and S2 (disordered), respectively. The region between 19° to 24° gives information about the quality of honeycomb ordering in α - Li_2IrO_3 (Fig. 6a, left inset). The black x-ray pattern with sharp and well-separated peaks indicates better honeycomb ordering and fewer stacking faults than the red x-ray pattern. A similar level of disorder carries over to the $\text{Ag}_3\text{LiIr}_2\text{O}_6$ produced from these precursors. We also reveal the effect of disorder on the magnetic behavior of α - Li_2IrO_3 by plotting DC susceptibility of both α - Li_2IrO_3 samples as a function of temperature below 60 K in the right inset of Fig. 6(a). The red curve does not show any signs of magnetic ordering while the black curve shows a peak at the AFM transition at 15 K.

Figure 6(b) shows the difference between the x-ray patterns of $\text{Ag}_3\text{LiIr}_2\text{O}_6$ samples S1 (black) and S2 (red). The main differences between the two samples are the intensity of the peak at 28.5° (left inset) and the sharpness in the asymmetric honeycomb peaks (right inset). S1 has sharper asymmetric honeycomb peaks and a shorter peak at 28.5° , which is similar to a prior report¹⁵. Whereas we have used AgNO_3 for the silver-exchange reaction, the authors of Ref.¹⁵ used a mixture of $\text{AgNO}_3/\text{KNO}_3$ for the reaction. In S2, the honeycomb peaks are broader and

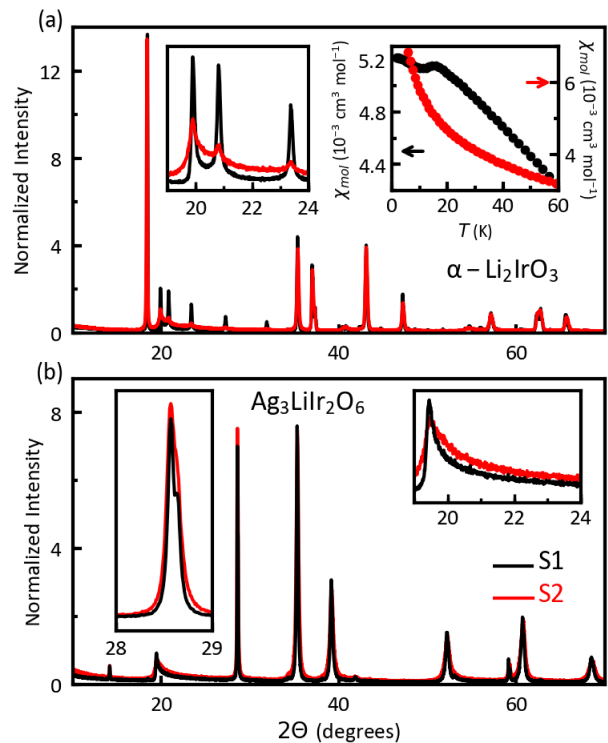


FIG. 6. (a) X-ray patterns of two α - Li_2IrO_3 precursors used in the synthesis of clean (black) and disordered (red) $\text{Ag}_3\text{LiIr}_2\text{O}_6$. The region of honeycomb peaks is magnified in the left inset. Temperature dependence of the DC magnetic susceptibility in the two α - Li_2IrO_3 precursors is presented in the right inset. (b) X-ray patterns of two $\text{Ag}_3\text{LiIr}_2\text{O}_6$, S1 (black) and S2 (the red pattern from Ref.¹⁴). The peak at 28.5° in the two $\text{Ag}_3\text{LiIr}_2\text{O}_6$ samples is compared in the left inset. The region of honeycomb peaks is magnified in the right inset.

the intensity of the two peaks at 28.5° and 35.3° are nearly the same.

Appendix B: Splitting between ZFC and FC data.

In Fig. 7, we show the splitting between ZFC and FC susceptibility at several fields. Note that the splitting persists to high fields, confirming a static spin freezing^{32,33} at T_N , as noted in the main text.

Appendix C: μSR data under longitudinal field.

In the main text, we derived $B_{\text{max}} = 269$ G in sample S1 at 0.28 K by fitting the zero-field (ZF) μSR data to a Bessel function (Eq. 3). As a consistency check, here we estimate the internal field B_{int} by analyzing the longitudinal field (LF) scans at 0.28 K as shown in Fig. 8(a). The initial polarization is fully recovered by 1000 G, so the internal field B_{int} must be much smaller than this

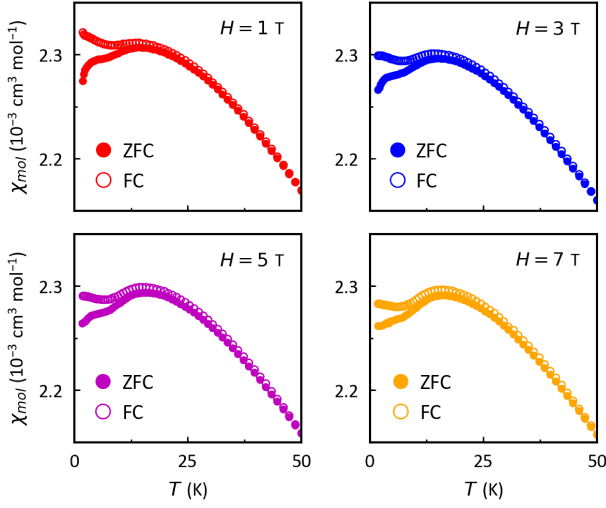


FIG. 7. The splitting between ZFC (full circles) and FC (open circles) susceptibility curves at 1, 3, 5, and 7 T.

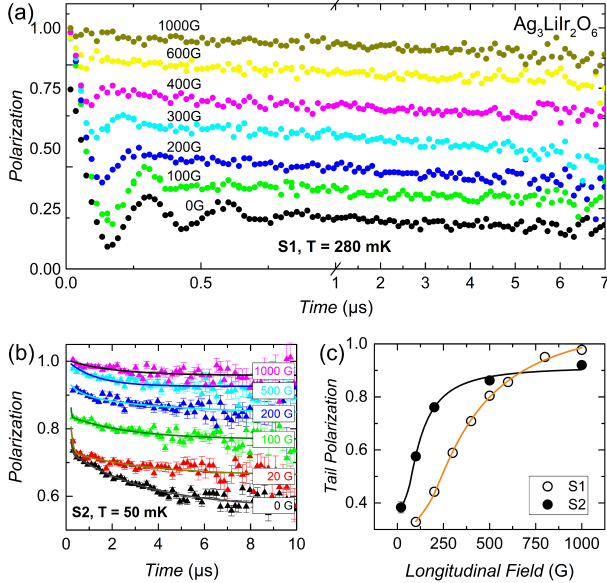


FIG. 8. (a) Polarization scans in the clean sample S1 at 0.28 K under different longitudinal fields (LF) from 0 to 1000 G. The time axis is expanded for $t < 1 \mu\text{s}$ to reveal the oscillations. (b) Polarization scans in the disordered sample S2 at 0.05 K under LF from 0 to 1000 G. The data in panels (a) and (b) were collected at the PSI and ISIS facilities, respectively. (c) By analyzing the recovery of the initial asymmetry with increasing field, we estimate $B_{\text{int}} = 263 \text{ G}$ in S1 and 113 G in S2. Solid lines are guides to the eye.

value. A detailed analysis³⁴ shows that the midpoint of the polarization recovery occurs at a field value close to $B/B_{\text{int}} = 4/3$. Figure 8(c) shows that the midpoint of recovery in S1 is at 350 G, yielding an internal field $B_{\text{int}} = 263 \text{ G}$, in good agreement with the $B_{\text{max}} = 269 \text{ G}$ obtained from our Bessel function fit to Eq. 3. We have

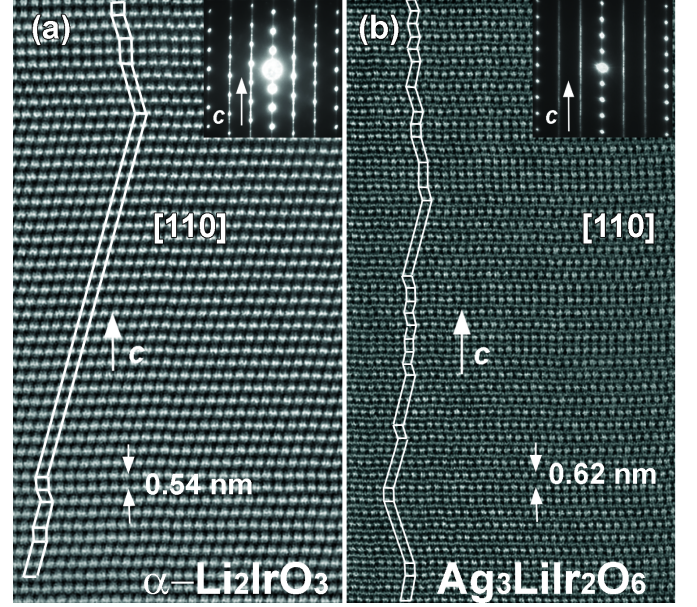


FIG. 9. HAADF-TEM images from (a) $\alpha\text{-Li}_2\text{IrO}_3$ and (b) $\text{Ag}_3\text{LiIr}_2\text{O}_6$ (S1). A clean sample is used for each material. The magnetization and X-ray data for the $\alpha\text{-Li}_2\text{IrO}_3$ sample are presented in Fig. 6 (black data). The magnetization data for the $\text{Ag}_3\text{LiIr}_2\text{O}_6$ are presented in the main text (sample S1). The images show an abundance of stacking faults in $\text{Ag}_3\text{LiIr}_2\text{O}_6$ unlike $\alpha\text{-Li}_2\text{IrO}_3$, due to the weaker interlayer coupling in the former. The ED patterns are presented as insets and reveal less streaking in $\alpha\text{-Li}_2\text{IrO}_3$ due to fewer stacking faults compared to $\text{Ag}_3\text{LiIr}_2\text{O}_6$.

also collected LF scans from the disordered sample S2 at 0.05 K as shown in Fig. 8(b). The midpoint of recovery in S2 occurs at 150 G in Fig. 8(c), yielding an internal field $B_{\text{int}} = 113 \text{ G}$ which is smaller than in sample S1. A smaller internal field may result from a range of muon stopping sites in the disordered sample. Since μSR is a local probe, we do not expect a major change in the local field near Ir^{4+} sites below T_N , but it is likely that muons probe a range of stopping sites with slightly different chemical environment due to various levels of Ag inclusion across the sample. This explains the slow depolarization of muons inside S2 at 10 K in Fig. 4, and the different polarization recovery between S2 and S1 in Fig. 8(c). As noted in the main text, it is not possible to fit the ZF data in sample S2 to a Bessel function (Eq. 3) because the oscillations are not discernible in the disordered sample. Thus, the LF analysis is the only way of estimating the local internal field in S2.

Appendix D: TEM analysis of the stacking faults.

Our discussion of the structural disorder in the main text is focused on the Ag inclusion within the honeycomb layers of $\text{Ag}_3\text{LiIr}_2\text{O}_6$ (Fig. 5). Here we point out that both the clean (S1) and disordered (S2) sam-

ples of $\text{Ag}_3\text{LiIr}_2\text{O}_6$ also suffer from the stacking faults, similar to other layered honeycomb materials such as $\text{Cu}_3\text{LiSn}_2\text{O}_6$ ²⁹. Figure 9 compares HAADF-TEM images between a clean sample of $\alpha\text{-Li}_2\text{IrO}_3$ and a clean sample of $\text{Ag}_3\text{LiIr}_2\text{O}_6$ (S1). There is no intersite disorder in either image, but $\text{Ag}_3\text{LiIr}_2\text{O}_6$ exhibits much more stacking faults than its parent compound $\alpha\text{-Li}_2\text{IrO}_3$. It has been demonstrated in a prior study of $\text{Cu}_3\text{LiSn}_2\text{O}_6$ that the stacking faults result from a twisting between the adjacent honeycomb layers, due to the weak O-Cu-O dumbbell bonds between the layers²⁹. A similar mechanism is at work in $\text{Ag}_3\text{LiIr}_2\text{O}_6$, where the weak O-Ag-O

dumbbell bonds lead to the twisting between the layers and produce the zig-zag stacking pattern observed in Fig. 9(b). Despite the considerable amount of stacking faults in sample S1 (Fig. 9(b)), it still shows clear signatures of long-range order as explained in the main text. In fact, the incommensurate order is similar between $\alpha\text{-Li}_2\text{IrO}_3$ and $\text{Ag}_3\text{LiIr}_2\text{O}_6$ based on our μSR data and the published results in Ref.³¹. Thus, we conclude that the magnetic interactions within the honeycomb layers are not affected by the interlayer bonds; however, they are disrupted by the extended defects in form of silver inclusion within the honeycomb layers.

-
- ¹ C. Broholm, R. J. Cava, S. A. Kivelson, D. G. Nocera, M. R. Norman, and T. Senthil, *Science* **367** (2020), 10.1126/science.aay0668.
 - ² J. Knolle and R. Moessner, *Annual Review of Condensed Matter Physics* **10**, 451 (2019), eprint: <https://doi.org/10.1146/annurev-conmatphys-031218-013401>.
 - ³ L. Savary and L. Balents, *Reports on Progress in Physics* **80**, 016502 (2016).
 - ⁴ A. Kitaev, *Annals of Physics January Special Issue*, **321**, 2 (2006).
 - ⁵ G. Jackeli and G. Khaliullin, *Physical Review Letters* **102**, 017205 (2009).
 - ⁶ Y. Singh, S. Manni, J. Reuther, T. Berlijn, R. Thomale, W. Ku, S. Trebst, and P. Gegenwart, *Physical Review Letters* **108**, 127203 (2012).
 - ⁷ H. Takagi, T. Takayama, G. Jackeli, G. Khaliullin, and S. E. Nagler, *Nature Reviews Physics* **1**, 264 (2019).
 - ⁸ K. W. Plumb, J. P. Clancy, L. J. Sandilands, V. V. Shankar, Y. F. Hu, K. S. Burch, H.-Y. Kee, and Y.-J. Kim, *Physical Review B* **90**, 041112 (2014).
 - ⁹ J. Nasu, J. Knolle, D. L. Kovrizhin, Y. Motome, and R. Moessner, *Nature Physics* **12**, 912 (2016).
 - ¹⁰ Y. Wang, G. B. Osterhoudt, Y. Tian, P. Lampen-Kelley, A. Banerjee, T. Goldstein, J. Yan, J. Knolle, H. Ji, R. J. Cava, J. Nasu, Y. Motome, S. E. Nagler, D. Mandrus, and K. S. Burch, *npj Quantum Materials* **5**, 1 (2020), number: 1 Publisher: Nature Publishing Group.
 - ¹¹ K. Kitagawa, T. Takayama, Y. Matsumoto, A. Kato, R. Takano, Y. Kishimoto, S. Bette, R. Dinnebier, G. Jackeli, and H. Takagi, *Nature* **554**, 341 (2018).
 - ¹² J. H. Roudebush, K. A. Ross, and R. J. Cava, *Dalton Transactions* **45**, 8783 (2016).
 - ¹³ M. Abramchuk, C. Ozsoy-Keskinbora, J. W. Krizan, K. R. Metz, D. C. Bell, and F. Tafti, *Journal of the American Chemical Society* **139**, 15371 (2017).
 - ¹⁴ F. Bahrami, W. Lafargue-Dit-Hauret, O. I. Lebedev, R. Movshovich, H.-Y. Yang, D. Broido, X. Rocquefelte, and F. Tafti, *Physical Review Letters* **123**, 237203 (2019).
 - ¹⁵ V. Todorova, A. Leineweber, L. Kienle, V. Duppel, and M. Jansen, *Journal of Solid State Chemistry* **184**, 1112 (2011).
 - ¹⁶ I. Kimchi, J. P. Sheckelton, T. M. McQueen, and P. A. Lee, *Nature Communications* **9**, 4367 (2018).
 - ¹⁷ J. Knolle, R. Moessner, and N. B. Perkins, *Physical Review Letters* **122**, 047202 (2019).
 - ¹⁸ Y. Choi, C. Lee, S. Lee, S. Yoon, W.-J. Lee, J. Park, A. Ali, Y. Singh, J.-C. Orain, G. Kim, J.-S. Rhyee, W.-T. Chen, F. Chou, and K.-Y. Choi, *Physical Review Letters* **122**, 167202 (2019).
 - ¹⁹ K. Mehlawat, A. Thamizhavel, and Y. Singh, *Physical Review B* **95**, 144406 (2017).
 - ²⁰ S. Widmann, V. Tsurkan, D. A. Prishchenko, V. G. Mazurenko, A. A. Tsirlin, and A. Loidl, *Physical Review B* **99**, 094415 (2019).
 - ²¹ A. Suter and B. M. Wojek, *Physics Procedia 12th International Conference on Muon Spin Rotation, Relaxation and Resonance ($\mu\text{SR}2011$)*, **30**, 69 (2012).
 - ²² S. Bette, T. Takayama, K. Kitagawa, R. Takano, H. Takagi, and R. E. Dinnebier, *Dalton Transactions* **46**, 15216 (2017).
 - ²³ E. M. Kenney, C. U. Segre, W. Lafargue-Dit-Hauret, O. I. Lebedev, M. Abramchuk, A. Berlie, S. P. Cottrell, G. Simutis, F. Bahrami, N. E. Mordvinova, G. Fabbri, J. L. McChesney, D. Haskel, X. Rocquefelte, M. J. Graf, and F. Tafti, *Physical Review B* **100**, 094418 (2019).
 - ²⁴ A. P. Ramirez, *Annual Review of Materials Science* **24**, 453 (1994).
 - ²⁵ J. Nasu, M. Udagawa, and Y. Motome, *Physical Review B* **92**, 115122 (2015).
 - ²⁶ A. Banerjee, P. Lampen-Kelley, J. Knolle, C. Balz, A. A. Aczel, B. Winn, Y. Liu, D. Pajerowski, J. Yan, C. A. Bridges, A. T. Savici, B. C. Chakoumakos, M. D. Lumsden, D. A. Tennant, R. Moessner, D. G. Mandrus, and S. E. Nagler, *npj Quantum Materials* **3**, 1 (2018).
 - ²⁷ A. Yaouanc and P. Dalmas de Réotier, *Muon Spin Rotation, Relaxation, and Resonance: Applications to Condensed Matter*, International Series of Monographs on Physics (Oxford University Press, Oxford, New York, 2011).
 - ²⁸ W.-H. Kao, J. Knolle, G. B. Halsz, R. Moessner, and N. B. Perkins, arXiv:2007.11637 [cond-mat] (2020).
 - ²⁹ M. Abramchuk, O. I. Lebedev, O. Hellman, F. Bahrami, N. E. Mordvinova, J. W. Krizan, K. R. Metz, D. Broido, and F. Tafti, *Inorganic Chemistry* **57**, 12709 (2018).
 - ³⁰ I. Rousochatzakis, S. Kourtis, J. Knolle, R. Moessner, and N. B. Perkins, *Physical Review B* **100**, 045117 (2019).
 - ³¹ S. Choi, S. Manni, J. Singleton, C. V. Topping, T. Lancaster, S. J. Blundell, D. T. Adroja, V. Zapf, P. Gegenwart, and R. Coldea, *Physical Review B* **99**, 054426 (2019).
 - ³² N. P. Raju, E. Gmelin, and R. K. Kremer, *Physical Review B* **46**, 5405 (1992).

- ³³ J. A. Mydosh, Reports on Progress in Physics **78**, 052501 (2015).
- ³⁴ F. L. Pratt, Journal of Physics: Condensed Matter **19**, 456207 (2007).